Effects of niobium on the microstructure, corrosion, and mechanical behavior of ultra-fine lamellar $Al_{0.3}CrFeCoNiNb_x$ eutectic high-entropy alloys

Zhenlong Liao [a], Ningning Li [a], Wei Yang [a], Shujie Pang [a,*], Nengbin Hua [b,*], Yang Meng [a], Peter K. Liaw [c], and Tao Zhang [a]

[a] *Key Laboratory of Aerospace Materials and Performance (Ministry of Education), School of Materials Science and Engineering, Beihang University, Beijing 100191, China*

[b] *Department of Materials Science and Engineering, Fujian University of Technology, 350118 Fuzhou, China*

[c] *Department of Materials Science and Engineering, The University of Tennessee, Knoxville, TN 37996, USA*

Abstract

This study investigates the effects of the element, Nb, on the microstructures, corrosion and mechanical behavior of the $Al_{0.3}CrFeCoNiNb_x$ (in molar ratio) high-entropy alloys (HEAs). It is found that the Nb addition facilitates the formation of the Nb-rich Laves phase for the HEAs. The HEAs show the microstructures of a hypoeutectic [the primary face-centered-cubic (FCC) phase] structure at x = 0.25 – 0.4, eutectic at x = 0.45, and hypereutectic (the primary Laves phase) phases at x = 0.5 – 0.75. In the 3.5 mass% NaCl solution, the $Al_{0.3}CrFeCoNiNb_x$ HEAs are spontaneously passivated and exhibit a low corrosion rate of less than 10^{-3} mm/year as a result of the formation of the protective passive films enriched in the chemically-stable Cr- and Nb-oxides. Compared with the FCC phase, the Laves phase displays a better corrosion resistance because of the higher concentration of Nb oxides in its passive film. The

$Al_{0.3}CrFeCoNiNb_{0.45}$ eutectic HEA possesses superior corrosion resistance among the HEAs, which is ascribed to a high concentration and more homogeneous distribution of Nb oxides in the passive film, as well as greater electrochemical impedance. Furthermore, the $Al_{0.3}CrFeCoNiNb_x$ HEAs with larger fractions of the Laves phase and ultra-fine eutectic structure present higher strength and hardness. Nevertheless, the plastic strain of the HEAs sharply decreases with increasing the amount of the brittle Laves phase. The results propose an effective approach for developing the HEAs with good corrosion resistance, high strength, and hardness.

Keywords： High-entropy alloy; Microstructure; Eutectic structure; Corrosion behavior; Mechanical property

*

E-mail addresses: pangshujie@buaa.edu.cn (S.J. Pang),

flower1982cn@126.com (N.B. Hua).

1. Introduction

In 2004, high-entropy alloys (HEAs) with a novel concept of alloy design were first proposed. This new alloy system was also defined as multi-principal component alloys [1][2]. In comparison with the conventional alloys that is characterized as single- or duplex-principal elements, HEAs generally consist of five or more principal elements, the concentrations of the constituent elements are between 5 atomic percent (at.%) and 35 at.% 0–**Error! Reference source not found.**. Because of their high configurational entropy of mixing in comparison with the traditional alloys, HEAs are usually composed of solid-solution phases 0–**Error! Reference source not found.**. The unique structural features of HEAs render them a variety of attractive properties, including good mechanical properties [5], high wear **Error! Reference source not found.**, and corrosion resistance [7]. Based on the multi-principal-component design concept, many novel HEAs with promising functional and structural performances have been developed in light-weight metal (Al, Mg, Li, Ti, etc.) systems [8][10], refractory metal (Mo, Nb, Ta, Hf, etc.) systems **Error! Reference source not found.Error! Reference source not found.–Error! Reference source not found.**, and Al-transition metal (Fe, Co, Cr, Ni, Mn, Ti, etc.) systems [15][15][16].

In the various HEAs, it displays the good mechanical properties and structural diversity for the Al-Cr-Fe-Co-Ni HEAs, which attracts widespread attention during the past decades [15][16]. For the $Al_xCrFeCoNi$ (in molar ratio) HEAs, as the Al content increases, the microstructure is composed of an face-centered-cubic (FCC) phase at x = 0 – 0.4, duplex FCC + BCC/ordered BCC (B2) phases at x = 0.5 – 0.8, and complete

BCC/B2 phases at x = 0.85 – 2.0 [16][17]. The microstructure evolution of the $Al_xCrFeCoNi$ HEAs exerts a significant influence on mechanical properties. As the Al content rises, the compressive yield strengths increase from 194 MPa at x = 0.3 to 400 MPa at x = 0.6, and to 1,400 MPa at x = 0.85, but it comes with a decrease in plastic strains from > 100% to 54%, and to 25% [17]. It is obvious that the $Al_xCrFeCoNi$ HEAs with FCC + BCC/B2 phases display both great strength and high ductility. A similar result is also obtained in the $AlCoCrFeNi_{2.1}$ eutectic HEA with the lamellar FCC + B2 phases, which exhibits a high ultimate tensile strength of 1,100 MPa and high ductility of 18% [18]. Nevertheless, the chemical segregations in different phases usually take place in the $Al_xCrFeCoNi$ HEAs with FCC + BCC/B2 phases. For example, the FCC phase possesses a higher content of Cr than the BCC/B2 phases [19][20]. Such chemical segregations in many HEAs always lead to the reduction in the corrosion resistance in the 3.5 mass% NaCl solution [18][20].

As is known to all, the chemical composition of the passive film is important to corrosion resistance [18]. The compact and protective passive films of alloys are the key factors to obtain high corrosion resistance **Error! Reference source not found.**[18]. A previous study found that the $Al_{0.3}Cr_xFeCoNi$ (x = 0 – 2.0) HEAs with a higher content of Cr show superior corrosion resistance in the 3.5 mass% NaCl solution, which is attributed to the increasing concentration of chemically-stable Cr-oxides in the protective passive films [7]. However, the $Al_{0.3}Cr_xFeCoNi$ HEAs display low yield strengths of 221 – 546 MPa when x = 0 – 2.0 [7]. It is widely accepted that both the high corrosion resistance and good mechanical properties of alloys can bring about an

advance in extensive applications, the further improvement of the corrosion resistance and strength for the Al-Cr-Fe-Co-Ni HEAs is a matter of vital importance.

Numerous studies revealed that many HEAs exhibit good corrosion resistance with the addition of the element, Nb, due to the formation of the chemically-stable Nb-oxide in protective passive films, such as the $Ni_{1.5}CrCoFe_{0.5}Mo_{0.1}Nb_x$ (x = 0.55 – 0.8) HEAs [22], $CoCrFeNiNb_x$ (x = 0.15 – 0.45) HEAs [23], and $(Ti_{1/3}Zr_{1/3}Hf_{1/3})_{15}(Nb_{1/2}Ta_{1/2})_x$ (x = 3 and 5) HEAs [13]. On the other hand, it is known that the element, Nb, has a larger radius than that of Cr, Fe, Co, and Ni [24]. Therefore, the solution of Nb into the Al-Cr-Fe-Co-Ni HEAs might result in the enhancement of the lattice-distortion energy, which leads to solid-solution strengthening. Meanwhile, Nb possesses relatively-large negative enthalpy of mixing with Al, Cr, Fe, Co, and Ni [$\Delta H_{mix\ (Nb\text{-}Al)} = -18$ kJ/mol, $\Delta H_{mix\ (Nb\text{-}Cr)} = -7$ kJ/mol, $\Delta H_{mix\ (Nb\text{-}Fe)} = -16$ kJ/mol, $\Delta H_{mix\ (Nb\text{-}Co)} = -25$ kJ/mol, and $\Delta H_{mix\ (Nb\text{-}Ni)} = -30$ kJ/mol)] [24]. The intermetallic compound usually forms in the Al-Cr-Fe-Co-Ni-Nb HEAs, which is beneficial to improve the strength and hardness [25][26]. Thus, the corrosion resistance, strength, and hardness of the Al-Cr-Fe-Co-Ni HEAs could be simultaneously improved with the addition of Nb.

The single-phase $Al_{0.3}CrFeCoNi$ HEA displays good ductility, while the strength is on the contrary [16][17]. As the Al content increases, the strength of the $Al_{0.3}CrFeCoNi$ HEA improves obviously because of the formation of the dual-phase structure, but it comes at a cost of the deterioration of corrosion resistance in NaCl solutions [16][17][19][20]. To simultaneously improve the corrosion resistance,

strength, and hardness, the element, Nb, was adopted into the $Al_{0.3}CrFeCoNi$ HEA. In this study, the $Al_{0.3}CrFeCoNiNb_x$ (x = 0.25, 0.35, 0.4, 0.45, 0.5, and 0.75 in molar ratio) HEAs were fabricated. We systematically studied the effects of Nb on the microstructure evolution, corrosion behavior, and mechanical properties of the $Al_{0.3}CrFeCoNiNb_x$ HEAs. The novel $Al_{0.3}CrFeCoNiNb_{0.45}$ eutectic HEA possessing that improved corrosion resistance, strength, and hardness was successfully developed. The $Al_{0.3}CrFeCoNiNb_{0.45}$ eutectic HEA with high content and uniform distribution of corrosion-resistant elements exhibited good corrosion resistance in the 3.5 mass% NaCl solution. The mechanism of high corrosion resistance of the eutectic HEA was discussed. Furthermore, the results offered the theoretical and experimental guidelines for the further applications of the HEAs.

2. Materials and methods

2.1 Materials preparation

Arc melting was employed to produce the alloy ingots of the $Al_{0.3}CrFeCoNiNb_x$ (x = 0.25, 0.35, 0.4, 0.45, 0.5, and 0.75 in molar ratio) HEAs using high-purity Al, Cr, Fe, Co, Ni, and Nb metals. The ingots were remelted at least four times under a Ti-gettered argon atmosphere. The tested samples were rods with a size of ϕ 6 mm × 50 mm using the injection copper mold casting under a high-purity argon atmosphere.

2.2 Microstructure characterization

The microstructure, which presents in the $Al_{0.3}CrFeCoNiNb_x$ HEAs, was characterized by D/MAX-2500 X-ray diffraction (XRD) using Cu-Kα radiation,

JSM7500 scanning electron microscopy (SEM), and FEI Tecnai G2 F20 transmission electron microscopy (TEM). The elemental distribution of the alloys was examined through the JSM7500 energy disperse spectroscopy (EDS). The volume fractions of the lamellar eutectic structures in the HEAs were determined by the software of Image J [27] from the SEM backscattered electron images. The thermal behavior of the $Al_{0.3}CrFeCoNiNb_{0.45}$ HEA was measured by the STA-449F3 differential scanning calorimeter (DSC) at the heating and cooling rates of 10 K/min. under an argon atmosphere.

2.3 Corrosion-behavior test

All of the electrochemical measurements of the $Al_{0.3}CrFeCoNiNb_x$ HEAs were performed in the 3.5 mass% NaCl solution using the Princeton VersaSTAT III electrochemical workstation. A three-electrode system was adopted to measure the electrochemical properties, where the working electrode was the sample, the reference electrode was the saturated calomel reference electrode (SCE), and the auxiliary electrode was the platinum. Before the tests of the potentiodynamic polarization and electrochemical impedance spectroscopy (EIS), the samples should be ensured that the open circuit potential (OCP) achieved a steady state after 1,800-second immersion. The potential sweep rate of the potentiodynamic-polarization test for all the alloys was 50 mV/min. The EIS measurement was performed at the OCPs of each HEAs. The disturbed voltage of the alternating current signal and the excitation frequency range of EIS were 10 mV and 10^5 – 10^{-2} Hz, respectively. After the 30-day immersion in the 3.5 mass% NaCl solution, the corrosion rate of the specimens was obtained as $R =$

$(87600\Delta W)/(S\rho t)$ (mm/year), where ΔW is the weight loss during immersion measured by an analytical balance (g, the precision is 0.01 mg), S is the surface area exposed in the NaCl solution (cm^2), ρ is the density (g/cm^3) measured by an Archimedean method [13], and t is the immersion time (h). The elemental characteristics of the surface films for the $Al_{0.3}CrFeCoNiNb_x$ HEAs (x = 0.25, 0.45, and 0.75) after the 24-hour immersion in the 3.5 mass% NaCl solution were measured by the ESCALABXi+ X-ray photoelectron spectroscopy (XPS) and analyzed by the XPSPEAK 4.1 software [28]. The corrosion tests were performed on the cross-section of the cylindrical samples. Before electrochemical measurements, all of the surfaces for the specimens were polished, using the 2,000-grit silicon carbide sandpaper and then exposed to air for about 24 h. The alloys' surface morphologies after potentiodynamic-polarization measurements were observed by SEM.

2.4 Mechanical properties test

The compression tests with a strain rate of 5×10^{-4} s^{-1} for the $Al_{0.3}CrFeCoNiNb_x$ HEAs were characterized by the SANS CMT5504 testing machine at room temperature. The size of the rod alloys for the compression tests is ϕ 6 mm × 12 mm. The fracture morphologies were investigated by SEM. The Vickers microhardness of the HEAs was measured by an FM800 Vickers hardness tester, using the load of 500 gf and the holding time of 15 s.

3. Results

3.1 Structural characterization

The XRD results of the $Al_{0.3}CrFeCoNiNb_x$ (x = 0, 0.25, 0.35, 0.4, 0.45, 0.5, and 0.75 in molar ratio) HEAs are depicted in Fig. 1. It is demonstrated that the Nb-free $Al_{0.3}CrFeCoNi$ HEA possesses a single FCC phase. According to the diffraction peaks of the Nb-bearing HEAs, the alloys with x > 0 present an FCC phase accompanied with a Laves phase. The SEM backscattered electron images of the $Al_{0.3}CrFeCoNiNb_x$ HEAs are explored to further study the characteristics of microstructures, as displayed in Fig. 2. It is clear that the $Al_{0.3}CrFeCoNiNb_x$ HEAs consist of a primary phase (the dark-contrast columnar region when x = 0.25 – 0.4, and the bright-contrast dendritic region when x = 0.5 – 0.75) and a typical lamellar eutectic structure. In the hypoeutectic alloys with x = 0.25 – 0.4, as the content of Nb rises, the amount of the dark-contrast columnar region gradually decreases, while the volume fraction of the lamellar eutectic structure significantly increases from 36% to 70%. When x = 0.45, only the lamellar eutectic structure can be found in the alloy. In the hypereutectic alloys with x = 0.5 – 0.75, as the Nb content rises, the amount of the bright-contrast dendritic region continuously rises, but that of the lamellar eutectic structure decreases from 85% to 27%. When x = 0.5 – 0.75, it is noteworthy that the bright-contrast dendritic region is surrounded by the large dark-contrast region with a width of 1 – 5 μm, and the width increases with the increasing content of Nb [29][30]. For the eutectic alloys, it has been proved that the mechanical properties are significantly related to the interlamellar spacing (λ) of the lamellar eutectic structure [31][32]. In the present $Al_{0.3}CrFeCoNiNb_x$ HEAs, the interlamellar spacings of the ultra-fine lamellar eutectic structure are $\lambda_{x=0.25}$ = 232 nm, $\lambda_{x=0.35}$ = 206 nm, $\lambda_{x=0.4}$ = 186 nm, $\lambda_{x=0.45}$ = 152 nm, $\lambda_{x=0.5}$ = 190 nm, and $\lambda_{x=0.75}$ =

280 nm, which are much finer than that of 700 nm for the $AlCoCrFeNb_xNi$ (x = 0 – 0.75) HEAs [25] and 1.5 μm for the $AlCoCrFeNi_{2.1}$ eutectic HEA [31][33].

Figure 3 shows the EDS mapping in the different contrast regions of the $Al_{0.3}CrFeCoNiNb_x$ HEAs. The elemental distribution reveals that Nb is enriched in the bright-contrast region, while Al, Cr, Fe, and Ni are enriched in the dark-contrast region. The Co uniformly distributes in the alloys. The crystal structures of the $Al_{0.3}CrFeCoNiNb_x$ HEAs with x = 0.25, 0.45, and 0.75 are further confirmed by the bright-field TEM images and the corresponding selected area electron diffraction (SAED) patterns, as presented in Figs. 4 (a–c). It is clear that the dark- and bright-contrast regions of the alloys correspond to the FCC and Laves phases, respectively. The DSC curves of the $Al_{0.3}CrFeCoNiNb_{0.45}$ HEA are plotted in Fig. 4(d). Only one endothermic peak is observed in the heating curves, which further evidences the eutectic composition of the $Al_{0.3}CrFeCoNiNb_{0.45}$ HEA. In summary, with the rising content of Nb, the microstructures of the $Al_{0.3}CrFeCoNiNb_x$ HEAs evolve from hypoeutectic (x = 0.25 – 0.4) to eutectic (x = 0.45), and to hypereutectic (x = 0.5 – 0.75) phases.

In order to investigate the phase stability in HEAs, the mixing enthalpy (ΔH_{mix}) [34] has been proposed as:

$$\Delta H_{\mathrm{mix}} = 4\sum_{i=1, i\neq j}^{n}\left(\Delta H_{ij}^{\mathrm{mix}} \cdot c_i \cdot c_j\right)$$

where the $\Delta H_{ij}^{\mathrm{mix}}$ is the enthalpy of mixing between the *i*-th and *j*-th elements, c_i and c_j are the atomic percents of the *i*-th and *j*-th elements, respectively. It is known that a more negative mixing enthalpy of an atomic pair indicates a stronger atomic bonding,

which tends to combine the atomic pair into intermetallic compounds [35]. In this study, the mixing enthalpy of the $Al_{0.3}CrFeCoNiNb_x$ HEAs are $\Delta H_{mix\ (x = 0)} = -5.27$ kJ/mol, $\Delta H_{mix\ (x = 0.25)} = -10.52$ kJ/mol, $\Delta H_{mix\ (x = 0.35)} = -11.62$ kJ/mol, $\Delta H_{mix\ (x = 0.4)} = -12.13$ kJ/mol, $\Delta H_{mix\ (x = 0.45)} = -12.61$ kJ/mol, $\Delta H_{mix\ (x = 0.5)} = -13.07$ kJ/mol, and $\Delta H_{mix\ (x = 0.75)} = -15.08$ kJ/mol. The $Al_{0.3}CrFeCoNiNb_x$ HEAs with a higher content of Nb display more negative mixing enthalpies, which are responsible for the formation of the Laves phase.

3.2 Corrosion behavior

Figure 5 summarizes the surface-morphology characteristics of the $Al_{0.3}CrFeCoNiNb_x$ HEAs immersed in the 3.5 mass% NaCl solution for 30 days. The typical polished surface morphologies of the alloys before the immersion are exhibited in Fig. 5(a). Figures 5(b)–(h) show the surface morphologies of the alloys after immersion, and the polished surfaces of the alloys have no visible changes. Moreover, the alloys have no detectable mass loss after immersion, implying that the alloys display a low corrosion rate (R) of less than 10^{-3} mm/year. These results indicate that the $Al_{0.3}CrFeCoNiNb_x$ HEAs possess high corrosion resistance.

The electrochemical measurements of the $Al_{0.3}CrFeCoNiNb_x$ HEAs were conducted in the 3.5 mass% NaCl solution, including the open circuit potentials (OCPs) and potentiodynamic polarization, as plotted in Fig. 6. Table 1 lists the corrosion potentials (E_{corr}), pitting corrosion potentials (E_{pit}), and corrosion current densities (i_{corr}) of the $Al_{0.3}CrFeCoNiNb_x$ HEAs. In Fig. 6 (a), for all the alloys, it is clear that the open circuit potentials initially increase with the extension of immersion time, and then

achieve relatively stable values. The results demonstrate that the surface films become more and more stable during immersion. From Fig. 6 (b), the $Al_{0.3}CrFeCoNiNb_x$ HEAs have the corrosion-current densities of 10^{-5} – 10^{-4} A/m^2. With further increase in the anodic potential, the HEAs are spontaneously passivated. At the anodic potentials of 0.573 – 1.018 V, the HEAs suffer pitting corrosion. As summarized in Table 1, when x = 0.25 – 0.45, the corrosion potentials and pitting-corrosion potentials of the alloys gradually increase with the rising Nb content. However, as the Nb content further rises to x = 0.5 and 0.75, the corrosion potentials and pitting-corrosion potentials of the alloys display a decreasing trend. As depicted in Fig. 7, pits with different sizes are observed on the alloys after potentiodynamic polarization, which agrees with the occurrence of pitting corrosion in the potentiodynamic-polarization curves. Besides, the FCC phase presents severer corrosion than the Laves phase, suggesting that the Laves phase possesses higher corrosion resistance. Thus, the $Al_{0.3}CrFeCoNiNb_{0.45}$ HEA shows superior corrosion resistance among the HEAs.

To further illustrate the corrosion mechanisms of the $Al_{0.3}CrFeCoNiNb_x$ HEAs, the measurement of EIS was conducted at the OCP of each alloy. The Nyquist plots of the alloys summarized in Fig. 8(a) exhibit a similar semicircle arc with different radii. As the Nb content rises (x = 0.25 – 0.45), the semicircle arc radii show an increasing trend. Conversely, as the Nb content further rises to x = 0.75, the semicircle arc radii gradually decrease. The Nyquist plots with larger semicircle arc radii indicate the higher impedance ($|Z|$) of the passive films, which is beneficial to achieving better corrosion resistance of the alloys. Figure 8(b) presents the Bode plots of the $Al_{0.3}CrFeCoNiNb_x$

HEAs in the frequency (f) range of 10^{-2} – 10^{5} Hz. When $f = 10^{-2}$ – 10^{4} Hz, the linear relationship between the impedance and frequency is associated with the pseudocapacitive nature of the passive films [36]. The alloys possess high impedance values about 10^{5} – 10^{6} Ω·cm^2 at $f = 10^{-2}$ Hz (the impedance of a 304 stainless steel at $f = 10^{-2}$ Hz is about 10^{5} – 10^{6} Ω·cm^2 [37]), which are conducive to the obtainment of high corrosion resistance in the aggressive environment.

In Fig. 8(c), the equivalent electrical circuit model, $R_s(Q_c(R_c(Q_pR_p))$, is used for the fit of the EIS data [7][19], where the R_s is the electrolyte resistance, R_c is the charge-transfer resistance, R_p is the passive resistance, and the Q_c and Q_p correspond to the capacitance of the charge transfer and passive layer, respectively. Due to the surface heterogeneities and adsorption effects on the alloys, the ideal capacitance (Q) response is replaced by the constant phase element (CPE) as $Q = Z_{\mathrm{CPE}} = Y^{-1}(j\omega)^{-n}$, which is composed of the proportionality factor (Y), the imaginary unit (j), the angular frequency (ω), and the dispersion coefficient (n, in the range of − 1 to 1) [38]. The values of n = 1, 0, and − 1 of the CPE response denote the capacitor, resistor, and inductance, respectively. The fittings of the EIS possess good quality according to the chi-square values of 10^{-5} – 10^{-4}. Table 2 lists the equivalent electrical circuit parameters of the impedance spectroscopy. Clearly, when x = 0.25 – 0.45, the charge-transfer resistance and passive resistance of the alloys display an increasing trend with the rising Nb content. However, as the Nb content of the HEAs further rises to x = 0.75, the charge-transfer resistance and passive resistance gradually decrease. It is noted that the higher electrochemical impedance of the passive films on alloys indicates better corrosion

resistance in an aggressive solution [39]. The EIS results of the $Al_{0.3}CrFeCoNiNb_x$ HEAs are consistent with those of the potentiodynamic-polarization tests (Fig. 6).

As a further investigation of the corrosion behavior for the $Al_{0.3}CrFeCoNiNb_x$ HEAs, the chemical characteristics of the surface films for the alloys with x = 0.25, 0.45, and 0.75 were studied by XPS. Figure 9 plots the XPS full spectra and narrow scanning spectra of elements of O 1s, Al 2p, Cr $2p_{3/2}$, Fe $2p_{3/2}$, Co $2p_{3/2}$, Ni $2p_{3/2}$, and Nb 3d of the surface on the alloys, where the ox and m represent the oxidized state and metallic state, respectively. In Fig. 9 (a), the peaks of elements, C, O, Al, Cr, Fe, Co, Ni, and Nb, exist in the full spectra. As presented in Fig. 9(b), the spectra of O 1s consist of O^{2-} (ox), OH^-, and H_2O peaks. As seen in Figs. 9(c–h), it can be concluded that the surface films are composed of the oxides of the corresponding constituent elements. Figure 10 shows the nominal compositions and the cationic concentrations of the surface films. Compared with the corresponding nominal compositions, the surface films of the $Al_{0.3}CrFeCoNiNb_x$ HEAs possess higher concentrations of Al, Cr, and Nb cations, while the concentrations of the Fe, Co, and Ni cations to the contrary. Apparently, the high concentrations of the chemically stable Cr- and Nb-oxides in the passive films for the $Al_{0.3}CrFeCoNiNb_x$ HEAs are responsible for the high corrosion resistance.

3.3 Mechanical behavior

The compressive stress-strain curves of the $Al_{0.3}CrFeCoNiNb_x$ HEAs are plotted in Fig. 11. Table 3 summarizes the yield strength ($\sigma_{0.2}$), compressive strength (σ_{max}), plastic strain (ε_p), and Vickers microhardness (Hv). The Nb-free $Al_{0.3}CrFeCoNi$ HEA

exhibits a yield strength of 220 MPa, Vickers microhardness of 169 Hv, and plastic strain of > 50%. It can be known from Fig. 11 that the strength and Vickers microhardness of the alloys obviously improve but the plastic strains deteriorate with the addition of Nb. With the rising content of Nb (x = 0.25 – 0.4), the yield strengths, compressive strengths, and Vickers microhardness of the alloys increase from 585 MPa, 1,654 MPa, and 379 Hv to 1,036 MPa, 1,948 MPa, and 534 Hv, respectively, but the plastic strain sharply decreases from 21.6% to 8.7%. The alloy at x = 0.45 displays the high yield strength of 1,684 MPa, compressive strength of 2,524 MPa, and Vickers microhardness of 675 Hv, and plastic strain of 3.8%. With further increasing the Nb content to x = 0.75, the yield strength, compressive strength, Vickers microhardness, and plastic strain of the alloy decrease to 1,437 MPa, 2,355 MPa, 634 Hv, and 1.5%, respectively. The strengthening mechanisms of the $Al_{0.3}CrFeCoNiNb_x$ HEAs caused by the addition of Nb are discussed in more detail in a later section.

Figure 12 shows the fracture-surface morphologies of the $Al_{0.3}CrFeCoNiNb_x$ HEAs after compressive tests. For the alloys with x = 0.25 – 0.4, tearing ridges with different lengths on the fracture surfaces are detected. The lengths of tearing ridges gradually decrease with the increase in the Nb content. Only trench-like patterns are observed on the fracture surfaces in the $Al_{0.3}CrFeCoNiNb_{0.45}$ HEAs. When x = 0.5 and 0.75, tearing ridges disappear, while cleavages and microcracks become dominant. It indicates that the alloys with more content of Nb are brittler.

4. Discussion

4.1 Effects of Nb on the corrosion resistance of the $Al_{0.3}CrFeCoNiNb_x$ HEAs

The potentiodynamic-polarization results indicated that the Nb-containing $Al_{0.3}CrFeCoNiNb_x$ HEAs display better corrosion resistance than the Nb-free $Al_{0.3}CrFeCoNi$ HEA in the 3.5 mass% NaCl solution. It is widely known that alloys with the protective passive films enriched in Cr and Nb are conducive to better corrosion resistance in the aggressive environments [13][30]**Error! Reference source not found.**. The XPS results demonstrated that the present Nb-containing $Al_{0.3}CrFeCoNiNb_x$ HEAs possess a higher total content of Cr and Nb cations (about 55.32 at.% – 62.55 at.%) in the passive films than that of the Nb-free $Al_{0.3}CrFeCoNi$ HEA (about 31 at.% Cr cation) [7]. The higher concentrations of chemically stable Cr- and Nb-oxides in passive films contribute to the better corrosion resistance of the $Al_{0.3}CrFeCoNiNb_x$ HEAs.

The corrosion morphologies of the $Al_{0.3}CrFeCoNiNb_x$ HEAs after polarization demonstrated that the FCC phase suffered severer corrosion in comparison with the Laves phase. The results of EDS mapping suggest that both the FCC and the Laves phases of the $Al_{0.3}CrFeCoNiNb_x$ HEAs have the high contents of Cr, *i.e.,* 21.89 at.% – 24.52 at.% and 18.72 at.% – 21.99 at.%, respectively. Such high contents of Cr favor the formation of the passive films enriched in Cr oxides on the FCC and Laves phases [41]. On the other hand, the Nb contents in the Laves phase (9.43 at.% – 22.03 at.%) are much higher than those in the FCC phase (2.11 at.% – 6.07 at.%), which leads to a higher concentration of Nb in the passive films on the Laves phase [41]. Consequently, the Laves phase exhibited better corrosion resistance than that of the FCC phase.

For the $Al_{0.3}CrFeCoNiNb_x$ HEAs with x = 0.25 and 0.45, the total concentrations of the corrosion-resistant Cr and Nb cations in the passive films formed in the NaCl solution are similar (*i.e.,* 55.32% for x = 0.25 and 55.60% for x = 0.45). However, the alloy with x = 0.45 possesses better corrosion resistance than the x = 0.25 alloy. As the content of Nb increases, the increasing fraction of the ultra-fine eutectic structure for the HEAs promoted the more uniform distribution of Nb in the passive film, which improves the corrosion resistance. In addition, the passive film of the alloy with x = 0.75 has a higher total concentration of the corrosion-resistant Cr and Nb cations (about 62.55%) than that of the x = 0.45 alloy (about 55.60%). Nevertheless, the alloys with a more content of Nb displayed lower corrosion resistance. For the present HEAs with x = 0.5 – 0.75, the large FCC phase with a width of 1 – 5 μm is discovered around the primary Laves phase, as seen in Fig. 2. Meanwhile, as the Nb content rises, the width of the large FCC phase for the alloy increases. The distribution of the chemically-stable Nb-oxide in the passive films might be inhomogeneous due to the appearance of the large FCC phase, which should be the major cause of the decrease in the corrosion resistance for the x = 0.5 – 0.75 alloys. Obviously, in the present $Al_{0.3}CrFeCoNiNb_x$ HEAs, the homogeneous distribution of the Nb-oxide in the passive films is also essential to improve the corrosion resistance.

4.2 Relationship between the microstructures and mechanical properties of the alloys with different Nb contents

With increasing the content of Nb, the strength and Vickers microhardness of the $Al_{0.3}CrFeCoNiNb_x$ HEAs initially enhance and then decrease. The

$Al_{0.3}CrFeCoNiNb_{0.45}$ eutectic HEA displays the highest strength and Vickers microhardness among the alloys. Meanwhile, as the content of Nb rises, the plastic strain of the alloys sharply decreases. Studies show that the atomic radii of elements, Al, Cr, Fe, Co, Ni, and Nb, are 0.143 nm, 0.125 nm, 0.124 nm, 0.125 nm, 0.125 nm, and 0.143 nm, respectively [24]. Obviously, Nb possesses a larger atomic size than Cr, Fe, Co, and Ni. Therefore, Nb in the FCC phase of the $Al_{0.3}CrFeCoNiNb_x$ HEAs results in the solution strengthening by enhancing the lattice distortion [42]. It is known that in comparison with the FCC phase, the Laves phase with an HCP structure exhibits fewer slip systems, leading to hard and brittle characteristics [25][42][43]. As a result, with the rising content of Nb for the present $Al_{0.3}CrFeCoNiNb_x$ alloys, the strength and Vickers microhardness significantly improve owing to the increasing amount of the Laves phase. For the eutectic HEAs with the lamellar FCC and Laves phases, it has been found that dislocations usually accumulate in the FCC phase during deformation [44]. The boundary between the FCC and the Laves phases efficiently hinders the movement of dislocations, enhancing the strength and hardness [44][44]. In the present alloys, the rising amount of the lamellar eutectic structure should lead to more boundaries between the FCC and Laves phases, which contributes to the improvement in strength and hardness. For the eutectic alloys, the yield strength relates to the interlamellar spacing (λ) according to the Hall-Petch relationship, $\sigma = \sigma^* + k/\sqrt{\lambda}$, where σ^* is the frictional stress, and k is a constant [26][44]. In this study, the λ value of the ultra-fine lamellar eutectic structure in the $Al_{0.3}CrFeCoNiNb_x$ HEAs initially decreases from 232 nm to 152 nm with increasing the content of Nb from x = 0.25 to x

= 0.45, respectively, and then increases up to 280 nm with the further addition of Nb. Clearly, for the $Al_{0.3}CrFeCoNiNb_x$ HEAs, the improvement of the yield strength is partially attributable to the reduction in interlamellar spacings of the ultra-fine lamellar eutectic structures.

A previous study showed that the $AlCoCrFeNi_{2.1}$ eutectic HEA with the lamellar FCC and B2 phases exhibited both the high strength and decent ductility, where the ductility was enabled by the soft FCC phase, and the high strength was rendered by the hard B2 phase [45]. However, the deformability of the $AlCoCrFeNi_{2.1}$ eutectic HEA was limited by the hard B2 phase [45]. It is known that FCC or BCC crystal structures have at least 12 slip systems. Therefore, extensive plastic deformation is normally possible along the various slip systems of the alloys with an FCC or BCC structure. Conversely, the HCP structure has only 3 slip systems, the alloys with an HCP structure are normally brittle. In this investigation, the $Al_{0.3}CrFeCoNiNb_x$ HEAs with higher Nb contents contain more Laves phases with HCP structures, resulting in the sharp decrease in ductility. This feature could also be responsible for the fact that the $Al_{0.3}CrFeCoNiNb_{0.45}$ eutectic HEA does not show both the high strength and good ductility. Similar results were observed in other reported eutectic HEAs, such as $AlCoCrFeNi_{2.1}Nb_x$ (x = 0 – 0.5) HEAs [44] and $CoCrFeNiNb_x$ (x = 0 – 0.412) HEAs [42]. A further study on achieving and understanding the combination of high strength and ductility of eutectic HEAs is expected.

Thus, in the present study, we successfully developed the novel $Al_{0.3}CrFeCoNiNb_x$ HEAs with the Cr-rich FCC and Nb-rich Laves phase, and the alloys displayed the

improved corrosion resistance, strength, and hardness. The high content and uniform distribution of corrosion-resistant elements of the $Al_{0.3}CrFeCoNiNb_{0.45}$ eutectic HEA were responsible for the good corrosion resistance in the 3.5 mass% NaCl solution. Besides, the unique lamellar eutectic structure of the $Al_{0.3}CrFeCoNiNb_x$ HEAs played an important role in the improvement of strength and hardness. In conclusion, the results proposed an effective approach for designing the HEAs with good corrosion resistance, high strength and hardness. These results provide the theoretical and experimental guidelines for the further applications of the HEAs.

5. Conclusions

In the present work, the novel $Al_{0.3}CrFeCoNiNb_x$ (x = 0.25, 0.35, 0.4, 0.45, 0.5, and 0.75 in molar ratio) eutectic HEAs were fabricated. We also studied the microstructure, corrosion behavior, and mechanical properties of the $Al_{0.3}CrFeCoNiNb_x$ HEAs. The results offered the suggestions for developing the HEAs with good corrosion resistance, high strength and hardness. The main conclusions are described as follows:

(1) The Nb addition to the $Al_{0.3}CrFeCoNiNb_x$ HEAs facilitates the formation of the HCP-structure Laves phase. As the content of Nb increases, the microstructures of the HEAs evolve from hypoeutectic (x = 0.25 – 0.4, the primary FCC phase and eutectic structure) to eutectic (x = 0.45, the eutectic structure) and to hypereutectic (x = 0.5 – 0.75, the primary Laves phase and eutectic structure) phases. The interlamellar spacings of the ultra-fine eutectic structure decrease from 232 nm to 152 nm, as the Nb content rises from x = 0.25 to x = 0.45 and increases to 280 nm

when further increasing the Nb content to x = 0.75. The FCC phase possesses a higher content of Al, Cr, Fe, and Ni than the Laves phase, while the Nb is enriched in the Laves phase. The element, Co, uniformly distributes in the alloys.

(2) In the 3.5 mass% NaCl solution, the $Al_{0.3}CrFeCoNiNb_x$ HEAs are spontaneously passivated and display a high corrosion resistance of less than 10^{-3} mm/year because of the formation of the passive films enriched in chemically stable Cr- and Nb-oxides. Compared with the FCC phase, the Nb-rich Laves phase shows better corrosion resistance because of the higher concentration of Nb oxides in its passive films. As the Nb content approaches x = 0.45, the distribution of the Nb oxide in passive films gradually homogenizes, and the electrochemical impedance of the passive films increases. With increasing the Nb content, the corrosion resistance of the alloys initially improves (x = 0.25 – 0.45) and then decreases (x ≥ 0. 5).

(3) With increasing the content of Nb, the strength and Vickers microhardness of the $Al_{0.3}CrFeCoNiNb_x$ HEAs initially improve and then decrease. The $Al_{0.3}CrFeCoNiNb_{0.45}$ eutectic HEA displays the highest yield strength of 1,684 MPa, compressive strength of 2,524 MPa, and Vickers microhardness of 675 Hv. Meanwhile, the rising amount of the Laves phase causes the sharp decrease in the plastic strain from 21.6% to 1.5%.

CRediT authorship contribution statement

Zhenlong Liao: Methodology, Investigation, Data curation, Writing - original draft. **Ningning Li:** Investigation, Data curation. **Wei Yang:** Methodology, Writing - review & editing. **Shujie Pang:** Conceptualization, Methodology, Supervision, Writing

- review & editing, Resources, Funding acquisition. **Nengbin Hua:** Conceptualization, Methodology, Writing - review & editing. **Yang Meng:** Methodology, Writing - review & editing. **Peter K. Liaw:** Writing - review & editing. **Tao Zhang:** Resources, Supervision.

Acknowledgements

This study was financially supported by National Natural Science Foundation of China (Grant No. 51971007) and the 111 Project (Grant No. B17002). PKL very much appreciates the support from the National Science Foundation (DMR – 1611180, 1809640, and 2226508).

References

[1] J.W. Yeh, S.K. Chen, S.J. Lin, J.Y. Gan, T.S. Chin, T.T. Shun, C.H. Tsau, S.Y. Chang, Nanostructured high-entropy alloys with multiple principal elements: novel alloy design concepts and outcomes, Adv. Eng. Mater. 6 (2004) 299−303. https://doi.org/10.1002/adem.200300567.

[2] B. Cantor, I.T.H. Chang, P. Knight, A.J.B. Vincent, Microstructural development in equiatomic multicomponent alloys, Mater. Sci. Eng. A 375–377 (2004) 213–218. https://doi.org/10.1016/j.msea.2003.10.257.

[3] D.B. Miracle, O.N. Senkov, A critical review of high entropy alloys and related concepts, Acta Mater. 122 (2017) 448–511. https://doi.org/10.1016/j.actamat.2016.08.081.

[4] E.P. George, D. Raabe, R.O. Ritchie, High-entropy alloys, Nat. Rev. Mater. 4 (2019) 515−534. https://doi.org/10.1038/s41578-019-0121-4.

[5] W.D. Li, D. Xie, D.Y. Li, Y. Zhang, Y.F. Gao, P.K. Liaw, Mechanical behavior of high-entropy alloys, Prog. Mater. Sci. 118 (2021) 100777. https://doi.org/10.1016/j.pmatsci.2021.100777.

[6] A.K. Kasar, K. Scalaro, P.L. Menezes, Tribological properties of high-entropy alloys under dry conditions for a wide temperature range—a review, Materials 14 (2021) 5814. https://doi.org/10.3390/ma14195814.

[7] X.L. Yan, H. Guo, W. Yang, S.J. Pang, Q. Wang, Y. Liu. P.K. Liaw, T. Zhang, $Al_{0.3}Cr_xFeCoNi$ high-entropy alloys with high corrosion resistance and good mechanical properties, J. Alloys Compd. 860 (2021) 158436. https://doi.org/10.1016/j.jallcom.2020.158436.

[8] N.D. Stepanov, D.G. Shaysultanov, G.A. Salishchev, M.A. Tikhonovsky, Structure and mechanical properties of a light-weight AlNbTiV high entropy alloy, Mater. Lett. 142 (2015) 153–155. https://doi.org/10.1016/j.matlet.2014.11.162.

[9] R. Feng, M.C. Gao, C. Lee, M. Mathes, T.T. Zuo, S.Y. Chen, J.A. Hawk, Y. Zhang, P.K. Liaw, Design of light-weight high-entropy alloys, Entropy 18 (2016) 333. https://doi.org/10.3390/e18090333.

[10] R. Feng, M.C. Gao, C. Zhang, W. Guo, J.D. Poplawsky, F. Zhang, J.A. Hawk, J.C. Neuefeind, Y. Ren, P.K. Liaw, Phase stability and transformation in a light-weight high-entropy alloy, Acta Mater. 146 (2018) 280–293. https://doi.org/10.1016/j.actamat.2017.12.061.

[11] W.J. Wang, K.H. Yang, Q.T. Wang, P.Q. Dai, H. Fang, F.J. Wu, Q.H. Guo, P.K. Liaw, N.B. Hua, Novel Ti-Zr-Hf-Nb-Fe refractory high-entropy alloys for potential biomedical applications, J. Alloys Compd. 906 (2022) 164383. https://doi.org/10.1016/j.jallcom.2022.164383.

[12] N.B. Hua, W.J. Wang, Q.T. Wang, Y.X. Ye, S.H. Lin, L. Zhang, Q.H. Guo, J. Brechtl, P.K. Liaw, Mechanical, corrosion, and wear properties of biomedical Ti-Zr-Nb-Ta-Mo high entropy alloys,

J. Alloys Compd. 861 (2021) 157997. https://doi.org/10.1016/j.jallcom.2020.157997.

[13] W. Yang, S.J. Pang, Y. Liu, Q. Wang, P. K. Liaw, T. Zhang, Design and properties of novel Ti-Zr-Hf-Nb-Ta high-entropy alloys for biomedical applications, Intermetallics 141 (2022) 107421. https://doi.org/10.1016/j.intermet.2021.107421.

[14] Y.P. Lu, Y. Dong, S. Guo, L. Jiang, H.J. Kang, T.M. Wang, B. Wen, Z.J. Wang, J.C. Jie, Z.Q. Cao, H.H. Ruan, T.J. Li, A promising new class of high-temperature alloys: eutectic high-entropy alloys, Sci. Rep. 4 (2014) 6200. https://doi.org/10.1038/srep06200.

[15] Y.P. Wang, B.S. Li, M.X. Ren, C. Yang, H.Z. Fu, Microstructure and compressive properties of AlCrFeCoNi high entropy alloy, Mater. Sci. Eng. A 491 (2008) 154–158. https://doi.org/10.1016/j.msea.2008.01.064.

[16] W.R. Wang, W.L. Wang, S.C. Wang, Y.C. Tsai, C.H. La, J.W. Yeh, Effects of Al addition on the microstructure and mechanical property of $Al_xCoCrFeNi$ high-entropy alloys, Intermetallics 26 (2012) 44–51. https://doi.org/10.1016/j.intermet.2012.03.005.

[17] J. Joseph, N. Stanford, P. Hodgson, D.M. Fabijanic, Understanding the mechanical behaviour and the large strength/ductility differences between FCC and BCC $Al_xCoCrFeNi$ high entropy alloys, J. Alloys Compd. 726 (2017) 885–895. https://doi.org/10.1016/j.jallcom.2017.08.067.

[18] X.Z. Gao, Y.P. Lu, B. Zhang, N.N. Liang, G.Z. Wu, G. Sha, J.Z. Liu, Y.H. Zhao, Microstructural origins of high strength and high ductility in an $AlCoCrFeNi_{2.1}$ eutectic high-entropy alloy, Acta Mater. 141 (2017) 59–66. http://dx.doi.org/10.1016/j.actamat.2017.07.041.

[19] Y.Z. Shi, B. Yang, X. Xie, J. Brechtl, K.A. Dahmen, P.K. Liaw, Corrosion of $Al_xCoCrFeNi$ high-entropy alloys: Al-content and potential scan-rate dependent pitting behavior, Corros. Sci. 119 (2017) 33–45. http://dx.doi.org/10.1016/j.corsci.2017.02.019.

[20] Y.Z. Shi, J.K. Mo, F.Y. Zhang, B. Yang, P.K. Liaw, Y. Zhao, In-situ visualization of corrosion behavior of $Al_xCoCrFeNi$ high-entropy alloys during electrochemical polarization, J. Alloys Compd. 844 (2020) 156014. https://doi.org/10.1016/j.jallcom.2020.156014.

[21] V. Hasannaeimi, S. Mukherjee, Galvanic corrosion in a eutectic high entropy alloy, J. Electroanal. Chem. 848 (2019) 113331. https://doi.org/10.1016/j.jelechem.2019.113331.

[22] X. Wen, X.F. Cui, G. Jin, Y.F. Liu, Y. Zhang, X.R. Zhang, E.B. Liu, H.L. Tian, Y.C. Fang, Corrosion and tribo-corrosion behaviors of nano-lamellar $Ni_{1.5}CrCoFe_{0.5}Mo_{0.1}Nb_x$ eutectic high-entropy alloy coatings: The role of dual-phase microstructure, Corros. Sci. 201 (2022) 110305. https://doi.org/10.1016/j.corsci.2022.110305.

[23] M. Zhang, L. Zhang, P. Liaw, G. Li, R. Liu, Effect of Nb content on thermal stability, mechanical and corrosion behaviors of hypoeutectic $CoCrFeNiNb_\chi$ high-entropy alloys, J. Mater. Res. 33 (2018) 3276–3286. https://doi.org/10.1557/jmr.2018.103.

[24] A. Takeuchi, A. Inoue, Classification of bulk metallic glasses by atomic size difference, heat of mixing and period of constituent elements and its application to characterization of the main alloying element, Mater. Trans. 46 (2005) 2817–2829. https://doi.org/10.2320/matertrans.46.2817.

[25] S.G. Ma, Y. Zhang, Effect of Nb addition on the microstructure and properties of AlCoCrFeNi high-entropy alloy, Mater. Sci. Eng. A 532 (2012) 480–486. https://doi.org/10.1016/j.msea.2011.10.110.

[26] H. Jiang, L. Li, Z.L Ni, D.X. Qiao, Q. Zhang, H.M. Sui, Effect of Nb on microstructure and properties of $AlCoCrFeNi_{2.1}$ high entropy alloy, Mater. Chem. Phys. 290 (2022) 126631. https://doi.org/10.1016/j.matchemphys.2022.126631.

[27] W. Yang, Y. Liu, S.J. Pang, P.K. Liaw, T. Zhang, Bio-corrosion behavior and in vitro biocompatibility of equimolar TiZrHfNbTa high-entropy alloy, Intermetallics 124 (2020) 106845. https://doi.org/10.1016/j.intermet.2020.106845.

[28] Y.Z. Shi, L. Collins, R. Feng, C. Zhang, N. Balke, P.K. Liaw, B. Yang, Homogenization of $Al_xCoCrFeNi$ high-entropy alloys with improved corrosion resistance, Corrosion Science 133 (2018) 120−131. https://doi.org/10.1016/j.corsci.2018.01.030.

[29] M.D. Nave, A.K. Dahle, D.H. StJohn, Halo formation in directional solidification, Acta Mater. 50 (2002) 2837–2849. https://doi.org/10.1016/S1359-6454(02)00104-0.

[30] R. Li, J. Ren, G.J. Zhang, J.Y. He, Y.P. Lu, T.M. Wang, T.J. Li, Novel $(CoFe_2NiV_{0.5}Mo_{0.2})_{100-x}Nb_x$ eutectic high-entropy alloys with excellent combination of mechanical and corrosion properties, Acta Metall. Sin. -Engl. Lett. 33 (2020) 1046–1056. https://doi.org/10.1007/s40195-020-01072-6.

[31] I. Baker, M. Wu, Z.W. Wang, Eutectic/eutectoid multi-principle component alloys: A review, Mater. Charact. 147 (2019) 545–557. https://doi.org/10.1016/j.matchar.2018.07.030.

[32] C.S. Tiwary，P. Pandey，S. Sarkar，R. Das，K. Chattopadhyay, Five decades of research on the development of eutectic as engineering materials, Prog. Mater. Sci. 123 (2022) 100793. https://doi.org/10.1016/j.pmatsci.2021.100793.

[33] A. Nassar, A. Mullis, R. Cochrane, Z. Aslam, S. Micklethwaite, L. Cao, Rapid solidification of $AlCoCrFeNi_{2.1}$ high-entropy alloy, J. Alloys Compd. 900 (2022) 163350. https://doi.org/10.1016/j.jallcom.2021.163350.

[34] Y. Zhang, Y.J. Zhou, J.P. Lin, G.L. Chen, P.K. Liaw, Solid-solution phase formation rules for multi-component alloys, Adv. Eng. Mater. 10 (2008) 534–538.

http://dx.doi.org/10.1002/adem.200700240.

[35] X. Yang, Y. Zhang, Prediction of high-entropy stabilized solid-solution in multi-component alloys, Mater. Chem. Phys. 132 (2012) 233–238. http://dx.doi.org/10.1016/j.matchemphys.2011.11.021.

[36] M. Ray, V.B. Singh, Effect of Sulfuric Acid on Corrosion and Passivation of 316 SS in Organic Solution, J. Electrochem. Soc. 158 (2011) C359–C368. https://doi.org/10.1149/2.047111jes.

[37] Y. Qiu, S. Thomas, M.A. Gibson, H.L. Fraser, K. Pohl, N. Birbilis, Microstructure and corrosion properties of the low-density single-phase compositionally complex alloy AlTiVCr, Corros. Sci. 133 (2018) 386–396. https://doi.org/10.1016/j.corsci.2018.01.035.

[38] D.D. Macdonald, M.C.H. McKubre, Modern Aspects of Electrochemistry, Plenum Press, New York, 1982.

[39] A. Fu, B. Liu, W.J. Lu, B. Liu, J. Li, Q.H. Fang, Z.M. Li, Y. Liu, A novel supersaturated medium entropy alloy with superior tensile properties and corrosion resistance, Scripta Mater. 186 (2020) 381–386. https://doi.org/10.1016/j.scriptamat.2020.05.023.

[40] Y. Fu, J. Li, H. Luo, C.W. Du, X.G. Li, Recent advances on environmental corrosion behavior and mechanism of high-entropy alloys, J. Mater. Sci. Technol. 80 (2021) 217−233. https://doi.org/10.1016/j.jmst.2020.11.044.

[41] S. Shuang, Z.Y. Ding, D. Chung, S.Q. Shi, Y. Yang, Corrosion resistant nanostructured eutectic high entropy alloy, Corros. Sci. 164 (2020) 108315. https://doi.org/10.1016/j.corsci.2019.108315.

[42] W.H. Liu, J.Y. He, H.L. Huang, H. Wang, Z.P. Lu, C.T. Liu, Effects of Nb additions on the microstructure and mechanical property of CoCrFeNi high-entropy alloys, Intermetallics 60 (2015) 1–8. http://dx.doi.org/10.1016/j.intermet.2015.01.004.

[43] G. He, J. Eckert, W. Löser, M. Hagiwara, Composition dependence of the microstructure and the mechanical properties of nano/ultrafine-structured Ti-Cu-Ni-Sn-Nb alloys, Acta Mater. 52 (2004) 3035–3046. http://dx.doi.org/10.1016/j.actamat.2004.03.006.

[44] Z.Y. Ding, Q.F. He, D. Chung, Y. Yang, Evading brittle fracture in submicron-sized high entropy intermetallics in dual-phase eutectic microstructure, Scripta Mater. 187 (2020) 280–284. https://doi.org/10.1016/j.scriptamat.2020.06.032.

[45] Y.P. Lu, X.Z Gao, L. Jiang, Z.N. Chen, T.M. Wang, J.C. Jie, H.J. Kang, Y.B. Zhang, S. Guo, H.H. Ruan, Y.H. Zhao, Z.Q. Cao, T.J. Li, Directly cast bulk eutectic and near-eutectic high entropy alloys with balanced strength and ductility in a wide temperature range, Acta Mater. 124 (2017) 143−150. http://dx.doi.org/10.1016/j.actamat.2016.11.016.

Table 1 Electrochemical parameters of $Al_{0.3}CrFeCoNiNb_x$ HEAs in the 3.5 mass% NaCl solution.

$Al_{0.3}CrFeCoNiNb_x$	E_{corr} (V)	i_{corr} ($\times 10^{-4}$ A/m^2)	E_{pit} (V)
x = 0	−0.165 ± 0.010	5.87 ± 0.13	0.571 ± 0.016
x = 0.25	−0.165 ± 0.009	1.67 ± 0.11	0.711 ± 0.015
x = 0.35	−0.154 ± 0.011	1.31 ± 0.09	0.840 ± 0.017
x = 0.4	−0.155 ± 0.006	1.14 ± 0.08	0.972 ± 0.015
x = 0.45	−0.155 ± 0.008	1.11 ± 0.10	1.018 ± 0.012
x = 0.5	−0.162 ± 0.008	1.24 ± 0.10	0.913 ± 0.013
x = 0.75	−0.173 ± 0.009	1.56 ± 0.08	0.889 ± 0.017

Table 2 Electrical-equivalent-circuit values for the EIS data of the $Al_{0.3}CrFeCoNiNb_x$ HEAs.

$Al_{0.3}CrFeCoNiNb_x$	R_s ($\Omega \cdot cm^2$)	R_c ($\times 10^4$ $\Omega \cdot cm^2$)	R_p ($\times 10^5$ $\Omega \cdot cm^2$)	CPE_c Y ($\times 10^{-5}$ $\Omega^{-1} \cdot cm^{-2} \cdot s^n$)	n	CPE_p Y ($\times 10^{-6}$ $\Omega^{-1} \cdot cm^{-2} \cdot s^n$)	n	$\Sigma\chi^2$ $\times 10^{-4}$
x = 0.25	1.39	1.35	2.25	3.85	0.89	9.74	0.68	6.43
x = 0.35	1.46	2.39	2.47	3.40	0.92	8.69	0.53	1.02
x = 0.4	1.47	2.99	4.77	2.73	0.92	5.71	0.67	0.92
x = 0.45	1.45	4.81	7.79	2.49	0.91	3.85	0.63	1.15
x = 0.5	1.46	2.42	4.46	2.77	0.92	5.14	0.65	1.22
x = 0.75	1.45	1.81	2.79	3.74	0.91	5.85	0.63	1.15

Table 3 Mechanical properties of the $Al_{0.3}CrFeCoNiNb_x$ HEAs.

$Al_{0.3}CrFeCoNiNb_x$	Yield Strength $\sigma_{0.2}$ (MPa)	Compressive Strength σ_{max} (MPa)	Plastic Strain ε_p (%)	Vickers Microhardness Hv
x = 0	220 ± 25	–	> 50	169 ± 6
x = 0.25	585 ± 27	1,654 ± 21	21.6 ± 1.1	379 ± 13
x = 0.35	785 ± 31	1,777 ± 24	10.8 ± 1.7	448 ± 9
x = 0.4	1,036 ± 24	1,948 ± 36	8.7 ± 1.0	534 ± 9
x = 0.45	1,684 ± 28	2,524 ± 22	3.8 ± 1.7	675 ± 15
x = 0.5	1,671 ± 27	2,369 ± 33	1.7± 1.3	642 ± 18
x = 0.75	1,437 ± 26	2,355 ± 28	1.5 ± 1.4	634 ± 14

Fig. 1 XRD patterns of the $Al_{0.3}CrFeCoNiNb_x$ HEAs.

Fig. 2 SEM backscattered electron images taken from the cross-section of the $Al_{0.3}CrFeCoNiNb_x$ alloy rods.

Fig. 3 The EDS mapping of the $Al_{0.3}CrFeCoNiNb_x$ HEAs.

Fig. 4 Bright-field TEM images and the corresponding selected area electron diffraction (SAED) patterns of the $Al_{0.3}CrFeCoNiNb_x$ HEAs with (a) x = 0.25, (b) x = 0.45, and (c) x = 0.75; (d) DSC curves of the $Al_{0.3}CrFeCoNiNb_{0.45}$ HEA with the heating and cooling rates of 10 K/min.

Fig. 5 Surface morphologies of the $Al_{0.3}CrFeCoNiNb_x$ HEAs (a) before and (b-h) after 30-day immersion in the 3.5 mass% NaCl solution.

Fig. 6 (a) Changes in the open circuit potentials (OCPs) with the immersion time and (b) the potentiodynamic-polarization curves of the $Al_{0.3}CrFeCoNiNb_x$ HEAs in the 3.5 mass% NaCl solution.

Fig. 7 Surface morphologies of the $Al_{0.3}CrFeCoNiNb_x$ HEAs after potentiodynamic-polarization tests in the 3.5 mass% NaCl solution with the insets showing the pits at a high magnification.

Fig. 8 (a) Nyquist diagrams and (b) Bode plots of the $Al_{0.3}CrFeCoNiNb_x$ HEAs at the OCP, and (c) equivalent-electrical circuit for fitting the EIS data.

Fig. 9 (a) XPS full spectra, (b) O 1s, (c) Al 2p, (d) Cr $2p_{3/2}$, (e) Fe $2p_{3/2}$, (f) Co $2p_{3/2}$, (g) Ni $2p_{3/2}$, and (h) Nb 3d of the surface for the $Al_{0.3}CrFeCoNiNb_x$ (x = 0.25, 0.45, and 0.75) HEAs.

Fig. 10 The nominal compositions and the cationic concentrations of the surface films for the $Al_{0.3}CrFeCoNiNb_x$ (x = 0.25, 0.45, and 0.75) HEAs.

Fig. 11 Compressive stress-stain curves of the $Al_{0.3}CrFeCoNiNb_x$ HEAs.

Fig. 12 Fracture surfaces of the $Al_{0.3}CrFeCoNiNb_x$ HEAs.

Fig. 1

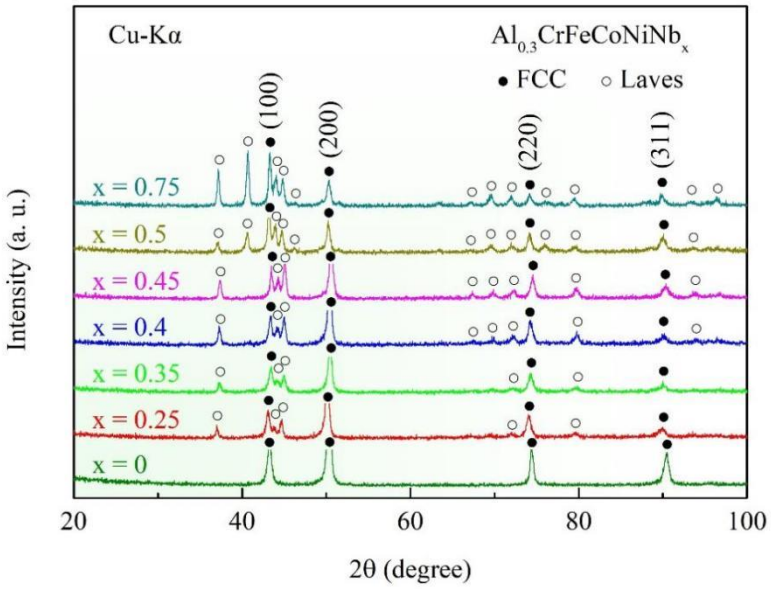
Cu-Kα
Al0.3CrFeCoNiNbx
• FCC ○ Laves
(100)
(200)
(220)
(311)
x = 0.75
x = 0.5
x = 0.45
x = 0.4
x = 0.35
x = 0.25
x = 0
Intensity (a. u.)
20
40
60
80
100
2θ (degree)

Fig. 2

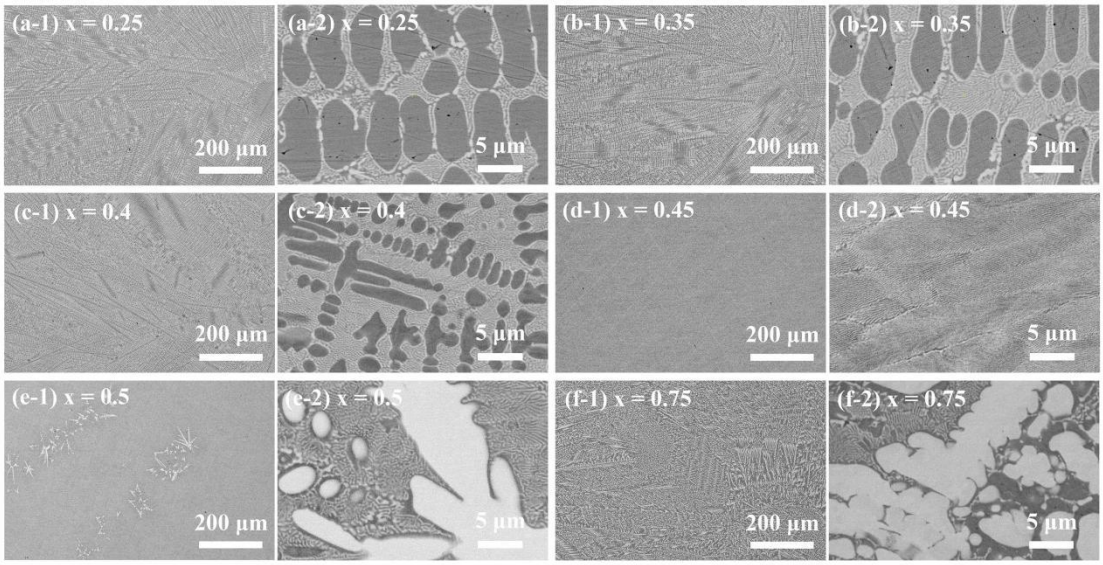
(a-1) x = 0.25
200 μm
(a-2) x = 0.25
5 μm
(b-1) x = 0.35
200 μm
(b-2) x = 0.35
5 μm
(c-1) x = 0.4
200 μm
(c-2) x = 0.4
5 μm
(d-1) x = 0.45
200 μm
(d-2) x = 0.45
5 μm
(e-1) x = 0.5
200 μm
(e-2) x = 0.5
5 μm
(f-1) x = 0.75
200 μm
(f-2) x = 0.75
5 μm

Fig. 3

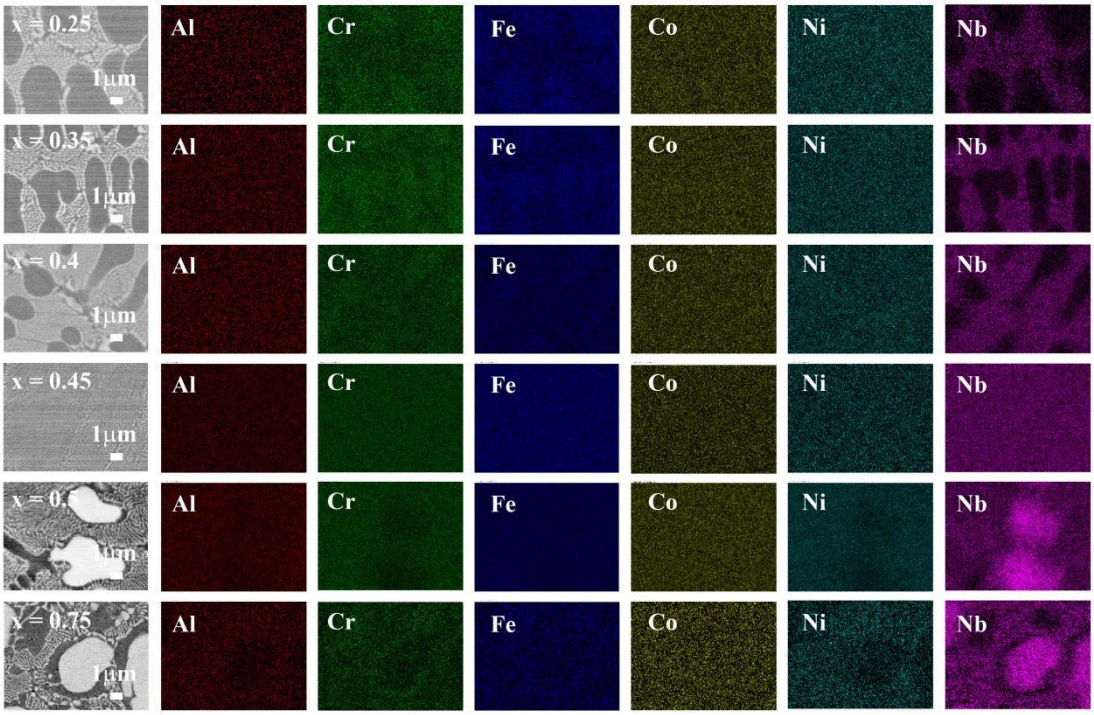
x = 0.25
1μm
Al
Cr
Fe
Co
Ni
Nb
x = 0.35
1μm
Al
Cr
Fe
Co
Ni
Nb
x = 0.4
1μm
Al
Cr
Fe
Co
Ni
Nb
x = 0.45
1μm
Al
Cr
Fe
Co
Ni
Nb
Al
Cr
Fe
Co
Ni
Nb
x = 0.75
1μm
Al
Cr
Fe
Co
Ni
Nb

Fig. 4

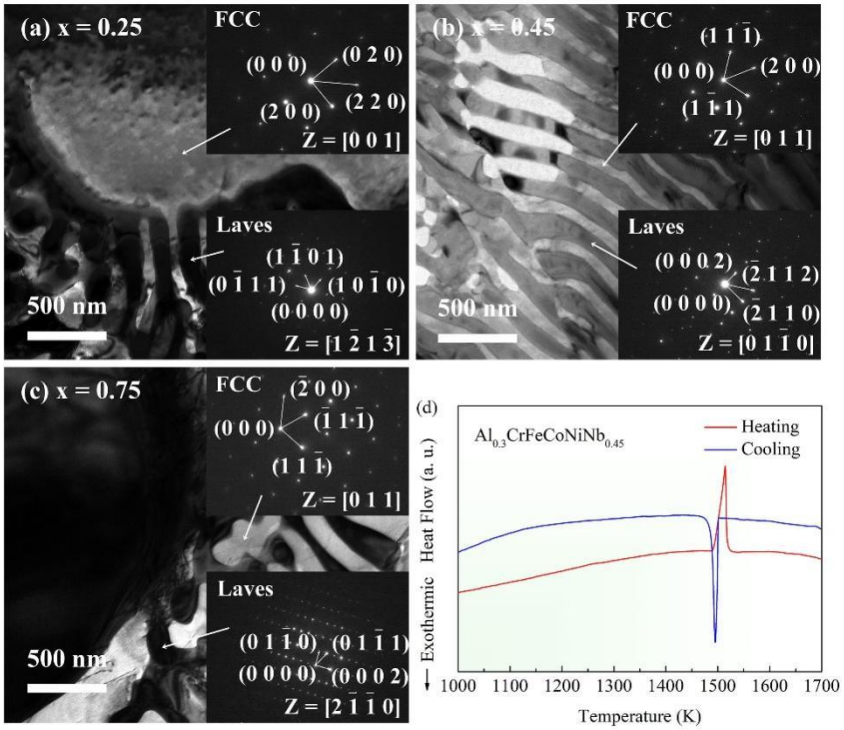
(a) x = 0.25
FCC
(0 0 0)
(0 2 0)
(2 0 0)
(2 2 0)
Z = [0 0 1]
Laves
(1 1̄ 0 1)
(0 1̄ 1 1)
(1 0 1̄ 0)
(0 0 0 0)
Z = [1 2̄ 1 3̄]
500 nm
(b) x = 0.45
FCC
(1 1 1̄)
(0 0 0)
(2 0 0)
(1 1̄ 1)
Z = [0 1 1]
Laves
(0 0 0 2)
(2̄ 1 1 2)
(0 0 0 0)
(2 1 1 0)
Z = [0 1 1̄ 0]
500 nm
(c) x = 0.75
FCC
(2̄ 0 0)
(0 0 0)
(1̄ 1 1̄)
(1 1 1̄)
Z = [0 1 1]
Laves
(0 1 1̄ 0)
(0 1 1̄ 1)
(0 0 0 0)
(0 0 0 2)
Z = [2 1̄ 1̄ 0]
500 nm
(d)
Al0.3CrFeCoNiNb0.45
Heating
Cooling
Exothermic Heat Flow (a. u.)
1000 1100 1200 1300 1400 1500 1600 1700
Temperature (K)

Fig. 5

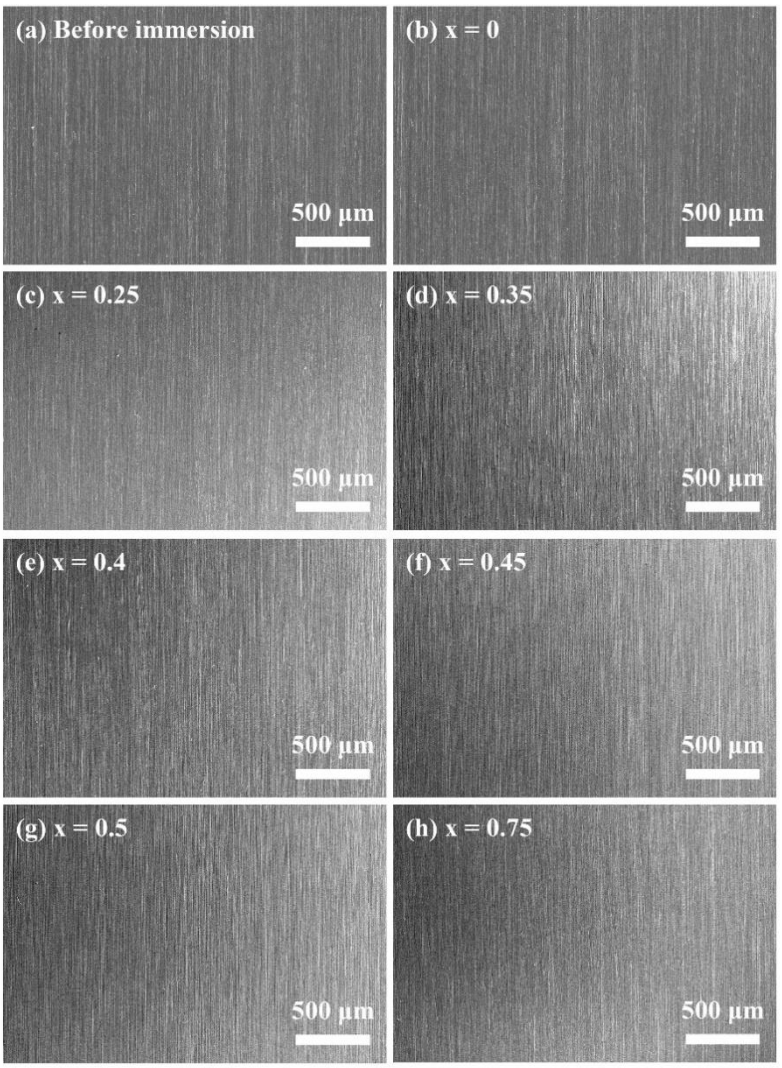
(a) Before immersion
500 μm
(b) x = 0
500 μm
(c) x = 0.25
500 μm
(d) x = 0.35
500 μm
(e) x = 0.4
500 μm
(f) x = 0.45
500 μm
(g) x = 0.5
500 μm
(h) x = 0.75
500 μm

Fig. 6

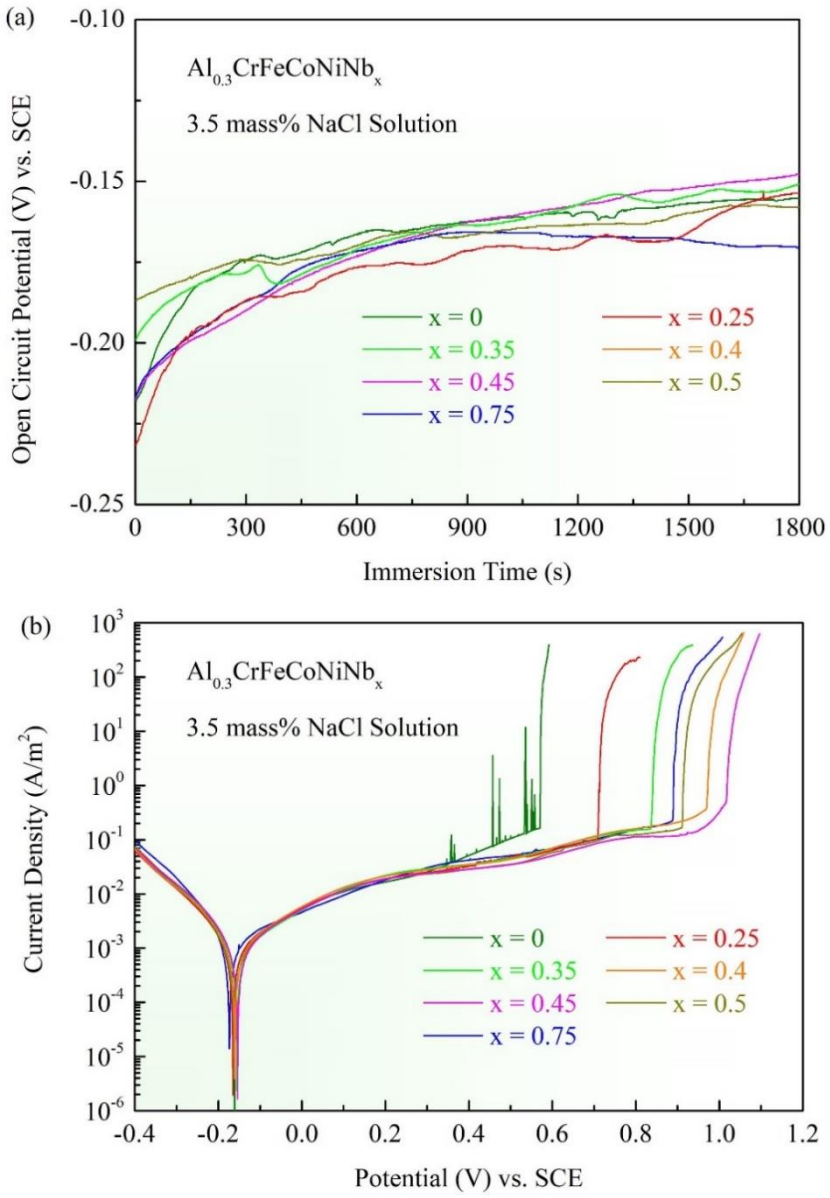
(a)
Al0.3CrFeCoNiNbx
3.5 mass% NaCl Solution
Open Circuit Potential (V) vs. SCE
Immersion Time (s)
x = 0
x = 0.25
x = 0.35
x = 0.4
x = 0.45
x = 0.5
x = 0.75
(b)
Al0.3CrFeCoNiNbx
3.5 mass% NaCl Solution
Current Density (A/m2)
Potential (V) vs. SCE
x = 0
x = 0.25
x = 0.35
x = 0.4
x = 0.45
x = 0.5
x = 0.75

Fig. 7

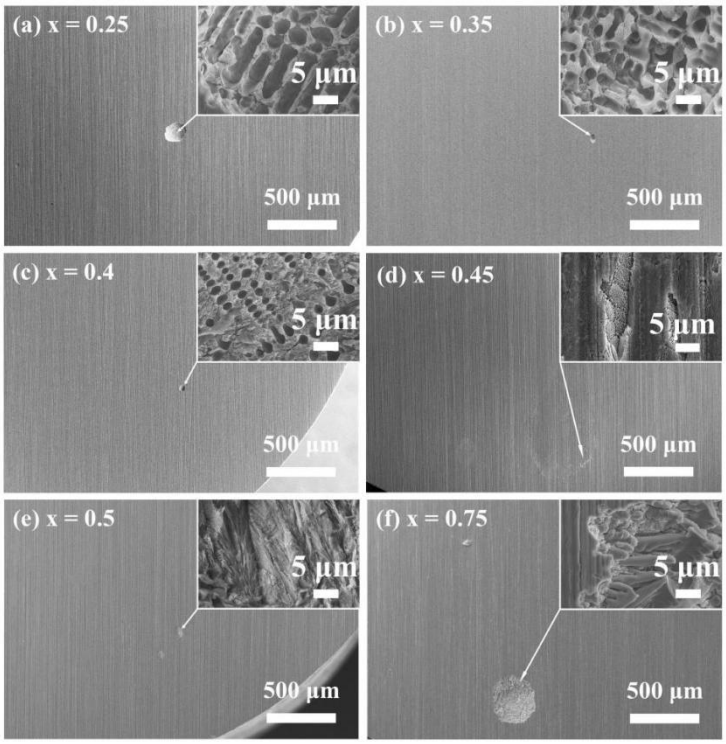
(a) x = 0.25
5 µm
500 µm
(b) x = 0.35
5 µm
500 µm
(c) x = 0.4
5 µm
500 µm
(d) x = 0.45
5 µm
500 µm
(e) x = 0.5
5 µm
500 µm
(f) x = 0.75
5 µm
500 µm

Fig. 8

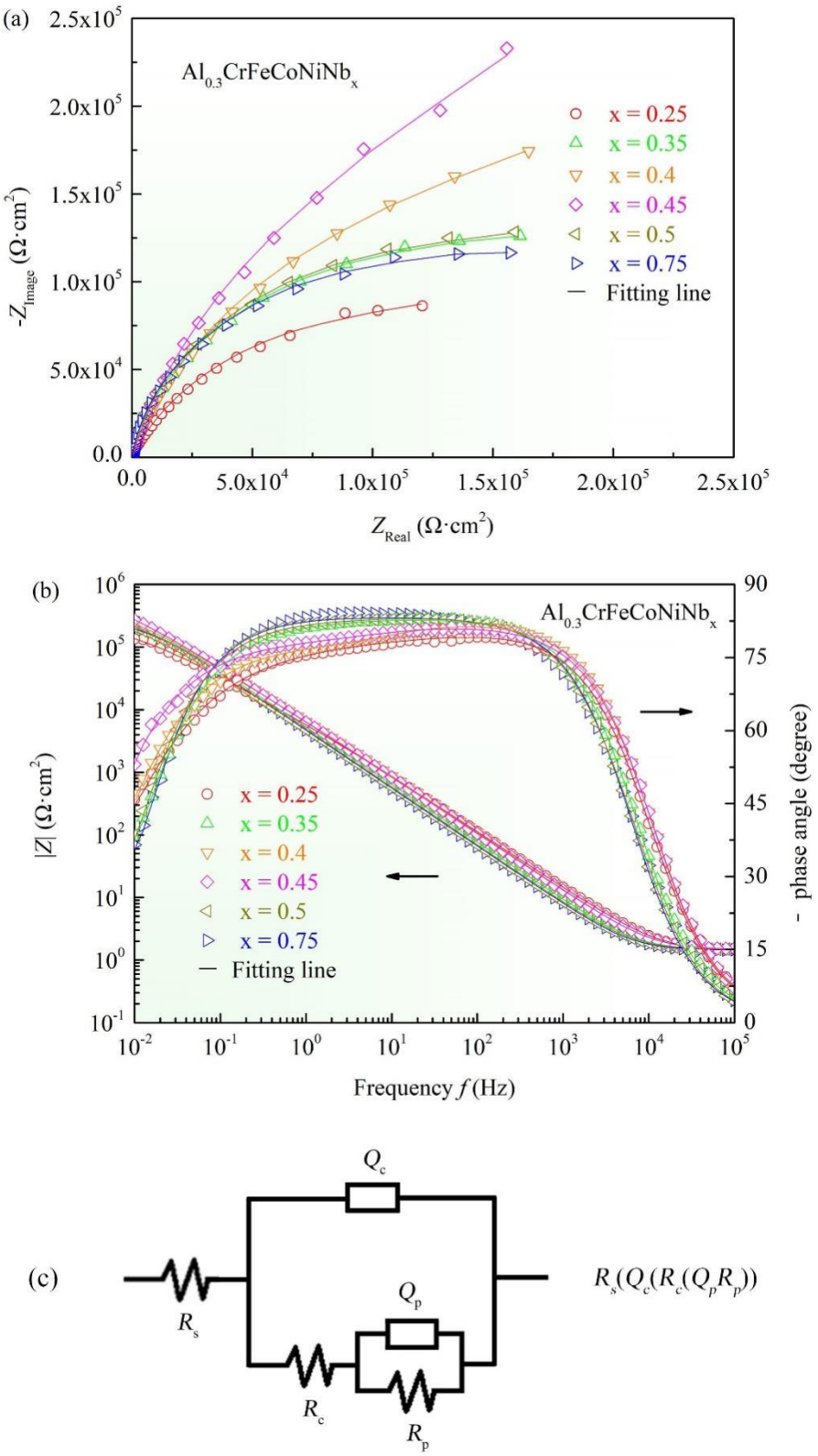
(a)
Al0.3CrFeCoNiNbx
x = 0.25
x = 0.35
x = 0.4
x = 0.45
x = 0.5
x = 0.75
Fitting line
-ZImage (Ω·cm2)
ZReal (Ω·cm2)
(b)
Al0.3CrFeCoNiNbx
|Z| (Ω·cm2)
- phase angle (degree)
Frequency f (Hz)
(c)
Qc
Rs
Qp
Rc
Rp
Rs(Qc(Rc(QpRp))

Fig. 9

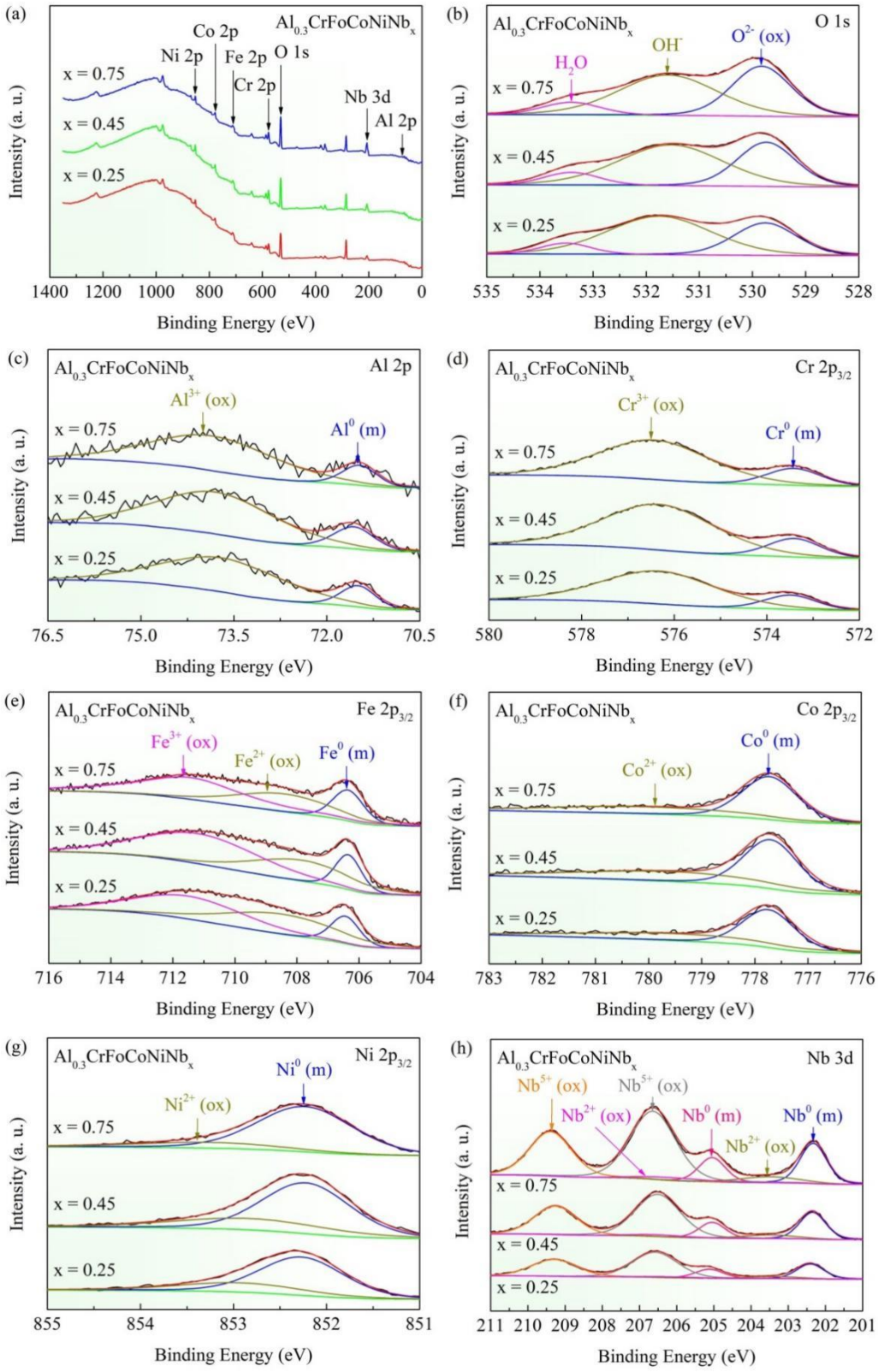
(a)
Al0.3CrFoCoNiNbx
Co 2p
Ni 2p
Fe 2p
O 1s
Cr 2p
Nb 3d
Al 2p
x = 0.75
x = 0.45
x = 0.25
Intensity (a. u.)
1400 1200 1000 800 600 400 200 0
Binding Energy (eV)
(b)
Al0.3CrFoCoNiNbx
O 1s
H2O
OH-
O2- (ox)
x = 0.75
x = 0.45
x = 0.25
Intensity (a. u.)
535 534 533 532 531 530 529 528
Binding Energy (eV)
(c)
Al0.3CrFoCoNiNbx
Al 2p
Al3+ (ox)
Al0 (m)
x = 0.75
x = 0.45
x = 0.25
Intensity (a. u.)
76.5 75.0 73.5 72.0 70.5
Binding Energy (eV)
(d)
Al0.3CrFoCoNiNbx
Cr 2p3/2
Cr3+ (ox)
Cr0 (m)
x = 0.75
x = 0.45
x = 0.25
Intensity (a. u.)
580 578 576 574 572
Binding Energy (eV)
(e)
Al0.3CrFoCoNiNbx
Fe 2p3/2
Fe3+ (ox)
Fe2+ (ox)
Fe0 (m)
x = 0.75
x = 0.45
x = 0.25
Intensity (a. u.)
716 714 712 710 708 706 704
Binding Energy (eV)
(f)
Al0.3CrFoCoNiNbx
Co 2p3/2
Co0 (m)
Co2+ (ox)
x = 0.75
x = 0.45
x = 0.25
Intensity (a. u.)
783 782 781 780 779 778 777 776
Binding Energy (eV)
(g)
Al0.3CrFoCoNiNbx
Ni 2p3/2
Ni0 (m)
Ni2+ (ox)
x = 0.75
x = 0.45
x = 0.25
Intensity (a. u.)
855 854 853 852 851
Binding Energy (eV)
(h)
Al0.3CrFoCoNiNbx
Nb 3d
Nb5+ (ox)
Nb5+ (ox)
Nb2+ (ox)
Nb0 (m)
Nb0 (m)
Nb2+ (ox)
x = 0.75
x = 0.45
x = 0.25
Intensity (a. u.)
211 210 209 208 207 206 205 204 203 202 201
Binding Energy (eV)

Fig. 10

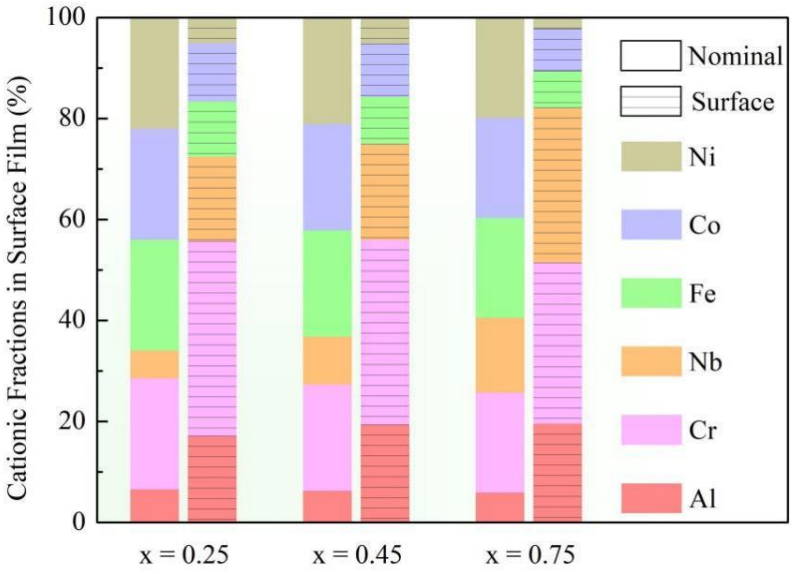
Cationic Fractions in Surface Film (%)
100
80
60
40
20
0
x = 0.25
x = 0.45
x = 0.75
Nominal
Surface
Ni
Co
Fe
Nb
Cr
Al

Fig. 11

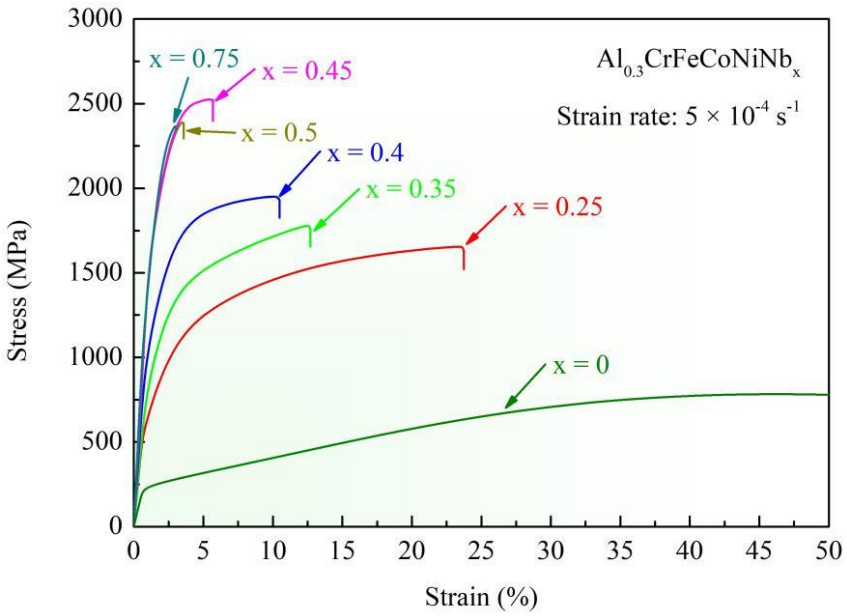
Al0.3CrFeCoNiNbx
Strain rate: 5 × 10-4 s-1
x = 0.75
x = 0.45
x = 0.5
x = 0.4
x = 0.35
x = 0.25
x = 0
Stress (MPa)
Strain (%)
0
500
1000
1500
2000
2500
3000
0
5
10
15
20
25
30
35
40
45
50

Fig. 12

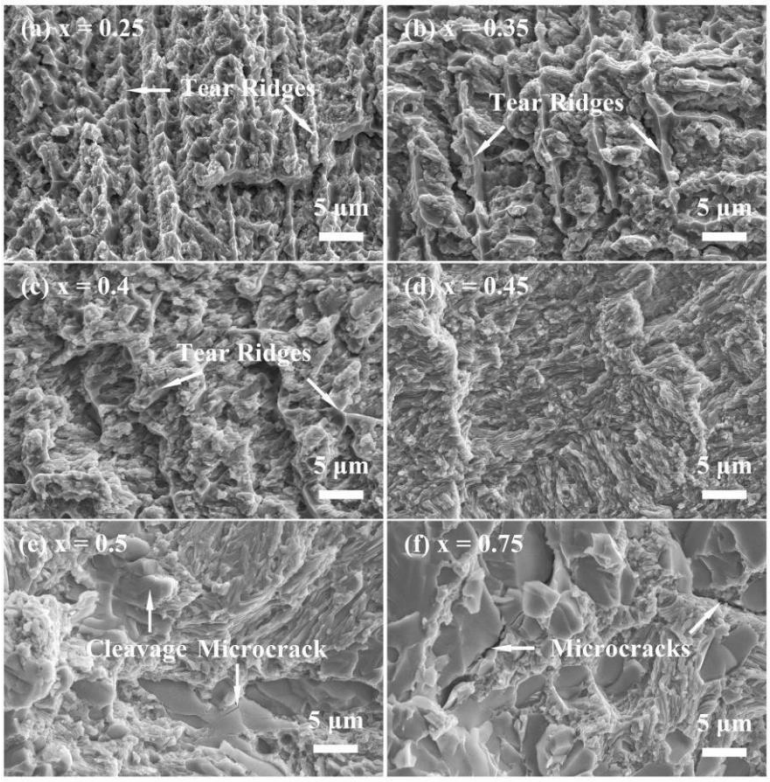
(a) x = 0.25
Tear Ridges
5 μm
(b) x = 0.35
Tear Ridges
5 μm
(c) x = 0.4
Tear Ridges
5 μm
(d) x = 0.45
5 μm
(e) x = 0.5
Cleavage Microcrack
5 μm
(f) x = 0.75
Microcracks
5 μm